Flow Simulation and Drag Anatomy for Antitank Projectile Configurations

Ameer G. Mikhail*
U.S. Army Ballistic Research Laboratory, Aberdeen Proving Ground, Maryland 21005-5066

Introduction

SPIKE-NOSED projectile configurations (Fig. 1) are fired against armored targets so that the spike acts as a stand-off distance between the armor and the shaped-charge warhead. The cone-nosed configurations, also shown in Fig. 1, may provide a windshield for reducing the drag, and provide a standoff distance as well. The lower drag for this cone-nosed class should extend the range for these projectiles, if launched at the same speed.

In prior studies,[1,2] computational results for spiked configurations with increasing geometrical complexity were presented. In Ref. 1, configurations of spikes with no vortex rings and bodies with no base-flow simulations were considered. In Ref. 2, the vortex generator ring was added and the body base flow was computed. The present work adds another degree of complexity, represented by an aftbody with steep boattail and tail fin boom. It thereby lays the foundation for the final step, which is the inclusion of fins on the tail boom.

The computations were made using the axisymmetric flow simulation code, using the zonal overlapping topology of Ref. 3. It uses the explicit, time-dependent McCormack numerical scheme. The purpose of this work is to provide the drag anatomy of each geometrical component of the projectile body, for both the spike- and the cone-nosed projectiles, at high supersonic speeds and zero angle of attack.

Projectile Geometries, Test Cases, and Test Conditions

Before computing a real projectile with fins, the logical preliminary progression was to test the computations on a one-step simpler configuration with the tail boom but without the fins. Experimental data were sought prior to performing the computations. Only wind-tunnel data were expected to exist, since without fins, these projectiles are statically unstable and may not be fired in a test range.

Two sets of wind-tunnel data were located. The first set[4] is for a spike-nosed projectile at transonic ($0.9 \leq M \leq 1.1$) and low supersonic ($M = 1.2$ and 1.4) speeds. This projectile is named configuration 1 in this study. Successful computations were made at $M = 3.5$ and 3. Attempts were made for computing the cases at $M = 1.2$ and 1.4, but yielded very large, unperiodic flow oscillations that were not indicated in Ref. 4; however, small oscillations were reported for a similar projectile in Ref. 5.

The second projectile configuration (configuration 2) is the actual 120-mm M830A1 multipurpose subcaliber projectile with the tail fin-boom but without the fins. The body diameter is 3.124 in. (80 mm). It has a biboattail with slopes of 12.5 and 4.5 deg. Computations were made at $M = 4.3$, 3.95, and 2.05. The range conditions are sea-level conditions of $p = 14.7$ psi and $T = 60°F$. The unit Reynolds numbers were 30.1, 27.6, and 14.3×10^6/ft for $M = 4.3$, 3.95, and 2.05, respectively. With no positive validation available for this configuration, a similar configuration (configuration 3), which has wind-tunnel data, was chosen next for computation and comparison.

The third configuration (configuration 3) is a 40%-scaled-down model of an earlier version of the M830A1 projectile. Wind-tunnel test results were available[6] in the second data reference. The tests were made in a 9-in. blowdown supersonic wind tunnel at $M = 3.5$ and 3. The model had a diameter of 1.261 in. and a biboattail with slopes of 20.5 and 4.6 deg. The tunnel total pressure was 75 and 60 psi, respectively. The total temperature was 60°F. The unit Reynolds number was 9.1 and 10.2×10^6/ft, respectively. No error bounds were given for these measurements. However, calibration errors on the tunnel balance were mentioned[6] as a possible error source.

Results

The governing equations, turbulence model, grid, and initial and boundary conditions were described in detail in Ref. 7. They are similar to those used in Refs. 1 and 2.

Flow Unsteadiness for Spiked Configurations

The work of Ref. 8 for range shadowgraph studies at transonic speeds of $M = 0.75$–1.24 has documented large-scale flow oscillations for both the low- and high-drag modes. These oscillations, similar to what Mikhail computationally reported[2] for $M = 1.9$, are due to the breakup and regeneration of vortices in the highly separated flow on the spike, behind the vortex generator ring. These oscillations are different from those that happen sometimes when the flow oscillates between the high- and low-drag modes. This latter type of oscillation was reported and studied by Calarese and Hankey[9] and Shang et al.[10] for a re-entry vehicle with a short spike. The former oscillations for a high- or low-drag case were encountered in the present work when the Mach number was lowered to $M = 1.9$, 1.4, and 1.2. Very large flow oscillations continued in the computations, and no steady flow pattern was observed. Biele,[5] also using firing-range shadowgraphs for spiked projectiles for Mach 0.9–3.5, indicated that the flow was unsteady because of vortex shedding from the vortex ring at Mach 1.4 and 2.6. However, the same projectile was also reported to have no flow unsteadiness when fired at either Mach 3.1 or 1.85. Biele indicates that there are at least three different flow patterns that the projectile goes through when decelerating from $M = 3.1$ to $M = 1.2$. The spike length, spike-to-body

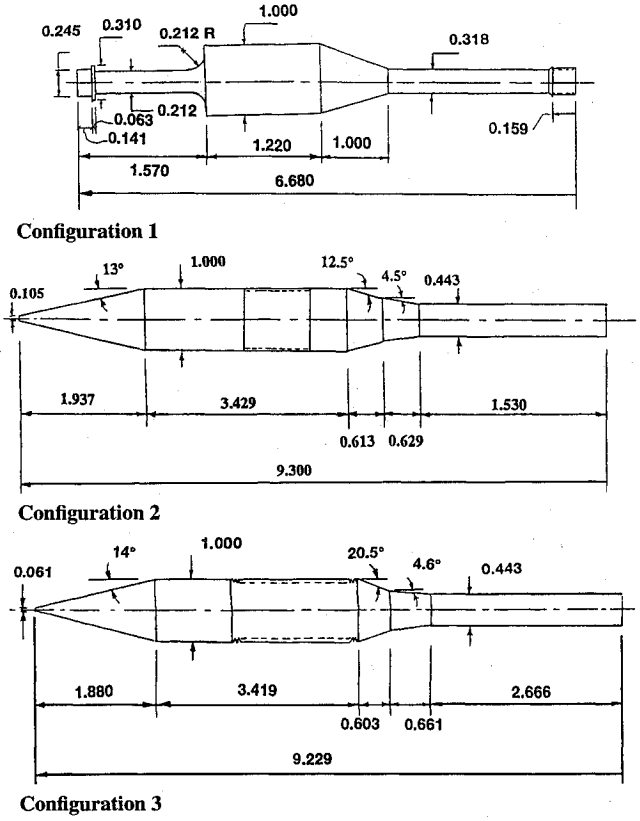

Fig. 1 Configurations of the three antitank projectiles. One caliber = 90 mm = 3.543 in. (configuration 1), one caliber = 80 mm = 3.124 in. (configuration 2), one caliber = 32 mm = 1.261 in. (configuration 3). Dimensions are in calibers.

Presented as Paper 94-0153 at the AIAA 32nd Aerospace Sciences Meeting, Reno, NV, Jan. 10–13, 1994; received Feb. 18, 1994; revision received Sept. 5, 1995; accepted for publication Sept. 11, 1995.

*Aerospace Engineer, Propulsion and Flight Division, Weapons Technology Directorate. Associate Fellow AIAA.

Table 1 Drag anatomy for configuration 1

Drag component	C_d, % $M = 3.5$	$M = 3.0$
Spike tip face	30.16	25.03
Vortex ring (both sides)	2.78	2.16
Main shoulder face	56.79	60.36
Boattail	10.23	12.19
Viscous drag (all body)	0.24	0.26
Total drag	100.00	100.00

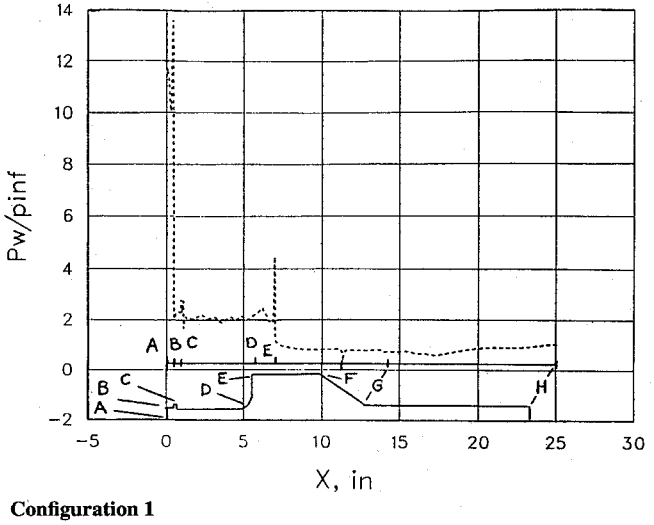

Configuration 1

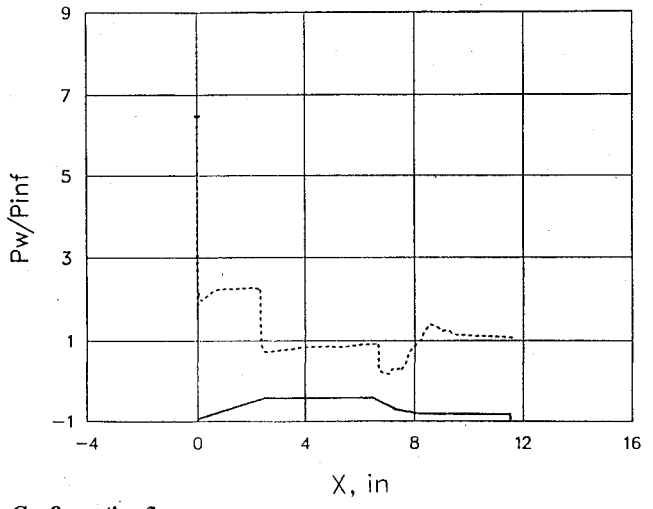

Configuration 3

Fig. 2 Computed surface pressure for configurations 1 and 3.

diameter ratio, and flow Reynolds and Mach numbers are the main parameters influencing the occurrence of these patterns.

Configuration 1

Computations were made for $M = 3.5$ and 3.0 using a wall-dense grid distribution with $\Delta y_1 = 1 \times 10^{-4}$ in. (2.5×10^{-3} mm). The flow exhibited small steady oscillations due to the breakup of vortices. The areas affected are the tip of the spike and the boattail regions. The flow was unsteady and not exactly periodic. The same flow unsteadiness was also reported[2] for a similar spiked-nose body.

The total forebody drag coefficient (total drag minus tail boom base drag) was 0.256 at $M = 3.0$ and decreased to 0.245 at $M = 3.5$. Figure 2 depicts the surface pressure distribution for $M = 3.5$. This case, not surprisingly, gave similar drag anatomy to that of $M = 3.0$. The drag anatomy for the two cases is listed in Table 1.

It is interesting to observe the very low viscous-drag percentage for the configuration. One is reminded that the flow is separated over the spike, the boattail, and most of the tail boom. Therefore, only the main body diameter and part of the tail boom, with its small surface area, contribute positively to the viscous drag.

Table 2 Drag anatomy for configuration 2

Drag component	C_d, % $M = 4.3$	$M = 3.95$	$M = 2.05$
Tip meplat face	7.60	7.25	4.31
Nose	64.10	61.79	51.19
Boattails	24.90	27.25	37.05
Viscous drag (all body)	2.61	2.76	3.29
Groove drag	0.79	0.95	4.16
Total drag	100.00	100.00	100.00

Table 3 Drag anatomy for configuration 3

Drag component	C_d, % $M = 3.5$	$M = 3.0$
Tip meplat face	1.90	1.75
Nose	60.06	56.67
Boattails	27.52	31.60
Viscous drag (all body)	8.25	7.27
Groove drag	2.27	2.71
Total drag	100.00	100.00

Configuration 2

Three cases, Mach 4.3, 3.95, and 2.05, were computed. Two grid spacing were tested to indicate the viscous-flow resolution near the body surface. The first grid spacing used as $\Delta y_1 = 0.005$ in., a very coarse distribution. The second was very fine and 50 times smaller, having $\Delta y_1 = 0.0001$ in. This test indicated no significant change in the total drag value.

The total forebody drag for the three cases was 0.2984, 0.1905, and 0.1796 for $M = 2.05$, 3.95, and 4.3, respectively. The groove drag was computed using the correlation of Ref. 11 and is included in the given values. The drag anatomy for $M = 4.3$ is listed in Table 2, together with the other two Mach numbers. The viscous drag is very small in this case because of the very high Reynolds number, which was 30.1×10^6/ft. This viscous drag value will triple when the Reynolds number decreases, as will be shown in the case of configuration 3. The groove drag for $M = 2.05$ is slightly high, since it is slightly outside the Mach speed range of Ref. 11. The drag components for the three cases are listed in Table 2.

Since the computations were not validated against experiment for this type of configuration, the following case of configuration 3, which is similar but has experimental data, was then computed for assurance.

Configuration 3

This 40%-scaled-down model was computed using the dense grid spacing with $\Delta y_1 = 0.0001$ in. (0.0025 mm) and the same number of grid points as in configuration 2. The two cases of Mach 3.5 and 3.0 were straightforwardly computed without difficulty. There were no unsteadiness in the flow. The computed total drag coefficient was 0.2668 at $M = 3.0$, compared to the measured value 0.253 of Ref. 4. For $M = 3.5$ the computed value was 0.2387, compared to 0.257 for the wind tunnel. This last wind-tunnel value is considered slightly in error, since it is greater than for $M = 3.0$. Usually the drag coefficient decreases with increasing Mach number, rather than increases. The present computation at $M = 3.5$ conforms and yields the correct trend.

The surface pressure is given in Fig. 2 for $M = 3.5$. The drag anatomy for the two cases is listed in Table 3.

Notice that the viscous drag has increased to 8.2% because of the lower Reynolds number than that of configuration 2. Also, the meplat drag is smaller than that of configuration 2 because of the smaller meplat.

Summary

Seven different cases were computed for three projectile configurations encompassing the two categories of antitank projectiles. Computations were made at both wind-tunnel and sea-level Reynolds numbers. The main features observed are summarized as follows:

1) The flow over a spike-nosed configuration (configuration 1) with vortex generator ring, boattail, and tail-fin boom was

computed at Mach 3.5 and 3.0 at a wind-tunnel Reynolds number of 4.5×10^6/ft and zero angle of attack. The computed flow features were consistent with the prior computations of Ref. 2. The new boattail and fin boom flow indicated that the vortex sheet (surface) extended over the boattail, thus inhibiting the usual wave expansion fan expected at the body–boattail junction.

2) The flow over the cone-nosed body of the M830A1 projectile with the 12.5- and 4.5-deg biboattails (configuration 2) was computed for Mach 4.3, 3.95, and 2.05 at sea-level Reynolds numbers of 30.1, 27.6, and 14.3×10^6/ft, respectively. The flow showed very small flow unsteadiness at the nose meplat at Mach 4.3, and it disappeared at Mach 2.05. There were evident expansion waves at the body–boattail junction due to the absence of the vortex sheet of a vortex ring.

3) The 40%-scaled-down model, a cone-nosed configuration of 20.5- and 4.6-deg biboattails (configuration 3), was computed at wind-tunnel Reynolds numbers of 9.1×10^6 and 10.2×10^6/ft for Mach 3.5 and 3.0, respectively. The axial force coefficient was compared with data, and indicated good agreement at Mach 3 and a measurement error at Mach 3.5, where the measured value increased rather than decreased, in contradiction of the normal trend.

4) The drag-component anatomy was examined for all cases computed. For the spiked cases, the spike tip and body shoulder contributed 25 and 60% of the total drag at $M = 3$. For the coned configuration (configuration 3), the nose and boattails contributed 57 and 32%, respectively, at Mach 3. No experiment, yet, has provided such an insight into the drag anatomy.

5) Contrary to the general expectation, the spike-nosed configuration drag was not much higher than the cone-nosed drag in the Mach 3.0–3.5 range. This finding is limited to spiked bodies with vortex generator rings, at the low-drag mode, at Mach $\geq$3.0. A spiked body without the ring can suffer much higher drag than the cone-nosed body at lower speeds ($M < 3$), especially in the spike high-drag mode.

6) The present computations indicated that these two classes of configurations can be successfully computed with the presented approach. This work, therefore, paves the way to computing the complete projectile configuration by including the fins.

References

[1]Mikhail, A. G., "Spiked-Nosed Projectiles: Computations and Dual Flow Modes in Supersonic Flight," *Journal of Spacecraft and Rockets*, Vol. 28, No. 4, 1991, pp. 418–424; AIAA Paper 89-1820.

[2]Mikhail, A. G., "Spike-Nosed Projectiles with Vortex Rings: Steady and Unsteady Flow Simulations," AIAA Paper 91-3261, Sept. 1991.

[3]Patel, N. R., and Sturek, W. B., "Multi-Tasked Numerical Simulation of Axisymmetric Ramjet Flows Using Zonal Overlapped Grids," U.S. Army Ballistic Research Lab., BRL-MR-3834, Aberdeen Proving Ground, MD, May 1990.

[4]Falkowski, E. W., "Static and Dynamic Stability Characteristics of the Supersonic Infantry Projectile at Transonic Velocities," U.S. Army Picatinny Arsenal, TM-1565, Dover, NJ, June 1965.

[5]Biele, J. K., "Drag and Flow Field Characteristics of Two Complex-Shaped Projectile Types," *Proceedings of the 7th International Symposium on Ballistics* (The Hague, The Netherlands), American Defence Preparedness Association, 1983, pp. 221–229.

[6]Farina, T., and Choudhary, A., "Wind Tunnel Test Results of an Advanced Multipurpose Tank Fired Projectile," U.S. Army Armament Research, Development and Engineering Center, ARDEC-TR-91015, Picatinny Arsenal, NJ, Oct. 1991.

[7]Mikhail, A. G., "Flow Simulation and Drag Anatomy for Anti-Tank Projectile Configurations," AIAA Paper 94-0153, Jan. 1994.

[8]Haupt, B. F., Buff, R. S., and Koening, K., "Aerodynamic Effects of Probe-Induced Flow Separation on Bluff Bodies at Transonic Mach Numbers," AIAA Paper 85-0103, Jan. 1985.

[9]Calarese, W., and Hankey, W. L., "Modes of Shock Wave Oscillations on Spike-Tipped Bodies," *AIAA Journal*, Vol. 23, No. 2, 1985, pp. 185–192.

[10]Shang, J. S., Hankey, W. L., and Smith, R. E., "Flow Oscillations of Spike-Tipped Bodies," *AIAA Journal*, Vol. 20, No. 1, 1982, pp. 25, 26.

[11]Mikhail, A. G., "Data Correlation and Surface Groove Drag for Kinetic Energy Projectiles," *Journal of Spacecraft and Rockets*, Vol. 26, No. 5, 1989, pp. 308–313; AIAA Paper 88–2541.

J. Allen
Associate Editor

Engineering Interactive Inviscid Boundary-Layer Method for Hypersonic Flow

Christopher J. Riley*
NASA Langley Research Center, Hampton, Virginia 23681
and
Fred R. DeJarnette†
North Carolina State University, Raleigh, North Carolina 27695

Introduction

ENGINEERING inviscid boundary layer methods[1–4] have been demonstrated to adequately predict the convective heating over a wide range of hypersonic vehicle geometries and aerothermal environments. Various approximations in the inviscid and boundary-layer regions enable a solution to be generated in a fraction of the time required by Navier–Stokes (NS), parabolized Navier–Stokes (PNS), viscous shock layer (VSL), or complete Euler/boundary-layer solvers. This reduction in computer time makes the engineering aerothermal methods ideal for parametric studies.

Although much effort has gone into developing coupled Euler/boundary layer codes[5–9] that allow interaction between the inviscid and viscous regions, the existing engineering methods follow a classical boundary-layer analysis. The inviscid flowfield influences the boundary-layer solution, but the viscous layer is assumed to have a negligible effect on the outer inviscid region. This assumption is accurate for relatively high Reynolds number flows where the boundary layer is thin compared to the shock layer. At lower Reynolds numbers, the thicker boundary layer displaces the outer flow and increases the surface pressure and heat transfer. Neglecting this displacement effect at lower Reynolds numbers may lead to inaccurate results.

To improve the capability of the engineering methods for lower Reynolds number flows, a current engineering aerothermal method has been modified to include the effects of viscous interaction. This algorithm is referred to as three-dimensional hypersonic inviscid boundary-layer method (THINBL).[10,11] It includes a simplified inviscid technique based on thin shock-layer theory for computing the three-dimensional outer flow,[12,13] a method of computing surface streamlines that allows the use of any axisymmetric boundary-layer technique for the viscous solution, and a set of approximate convective heating equations.[14] This Note outlines the viscous interaction procedure used in THINBL and demonstrates its effect on a spherically blunted cone at a representative low Reynolds number condition.

Analysis

This section briefly describes the engineering inviscid boundary-layer method THINBL. An outline of the viscous interaction procedure is also given. More details may be found in Refs. 10–13.

THINBL

The three-dimensional inviscid analysis[12,13] used in THINBL is simplified by using approximate stream functions in the shock layer and by using an explicit expression for the pressure across the shock

Received May 30, 1995; revision received July 28, 1995; accepted for publication Aug. 1, 1995.

*Aerospace Engineer, Aerothermodynamics Branch, Gas Dynamics Division. Member AIAA.

†Professor, Mechanical and Aerospace Engineering Department. Associate Fellow AIAA.